Chapter 5

EFFECTS OF THERMOMECHANICAL PROCESSING ROUTE

5.1 INTRODUCTION

The heat-treatable Al-Cu-Mg-Si (AA6061) alloy finds wide application as construction material in the transportation and building industry markets. The main advantage of this aluminium alloy is its high specific strength. However, commercial applications may be limited by poor characteristics such as a lower fracture toughness, which is known to depend on many parameters, e.g. intermetallic content, grain size and grain boundary structure and properties [1,2]. Susceptibility to intergranular corrosion attack, which increases with ageing time to a maximum at peak-aged condition, is favoured by precipitation at the grain boundaries [3]. Also, cases are known [4,5] in which size-effects of grain boundary precipitates may completely alter the mode of fracture.

The thermomechanical processing route is primarily responsible for the mechanical properties of aluminium alloys. As already described in Chapter 2, these alloys are solution heat treated, water-quenched and artificially aged. It can readily be understood that the quench-rate will vary along the cross-section of the extruded bars. Therefore its effects on grain boundary properties and fracture mechanics will be studied together with those of subsequent ageing time. In order to study the influences of microstructure, a recrystallized alloy is compared to an extruded alloy.

5.2 FRACTURE STRAIN IN RELATION TO GRAIN BOUNDARY PRECIPITATION

During an isothermal ageing sequence, many precipitation-hardening alloys exhibit a condition in which the interior of the grains is highly hardened while the grain boundary environment remains very soft (i.e. the precipitate free zone or PFZ). This softness finds its origin in a local depletion of vacancies and solute inhibiting the formation of a fine dispersion of particles in that region. Experiments indicate that the plastic strain can be highly localised inside these soft zones that circumvent the grain boundary. The interface between the relatively hard grain boundary precipitate and the soft grain boundary region may act as a preferred site for initiation and propagation of cracks. In this way, the alloy may fail according to an intergranular but ductile mechanism, often designated as intergranular-microvoid-coalescence. When grain interior and grain boundary region are of comparable hardness, concentration of strain at the grain boundary region is not pronounced and a more transgranular type of fracture is prevalent, usually transgranular-microvoid-coalescence. Fig 5.1 schematically depicts these different modes of failure.

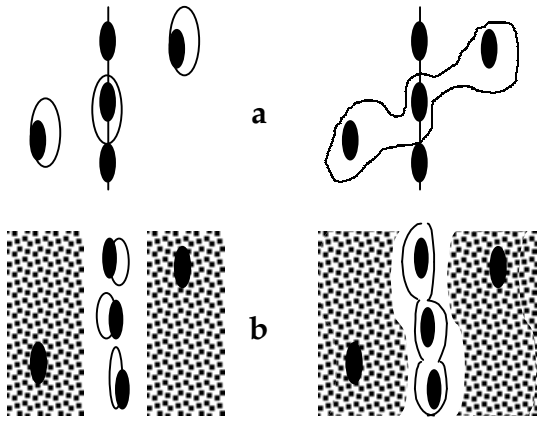

Fig 5.1: *Schematic representation of failure mechanisms in precipitation hardened alloys:*
(a) No localisation of strain at the grain boundary – transgranular microvoid coalescence
(b) Localisation of strain at the grain boundary – intergranular microvoid coalescence

Considered that in most precipitation hardening alloys incoherent precipitates form by heterogeneous nucleation at grain boundaries, it can be expected that their local volume portion f_i will lower the part of the fracture strain that is confined to the grain boundary region, ε_{fi}, according to [6-8]

$$\varepsilon_{fi} = \left(\sqrt{\frac{\pi}{6 f_i}} - \sqrt{\frac{2}{3}} + \varepsilon_n \right)^{\frac{1}{C}} - 1 \qquad (5.1)$$

where C ~ 1.5 is a factor accounting for the faster extension rate of voids as compared to the matrix before the critical condition of instability is reached and ε_n is a critical strain to nucleate a void at the interface of an incoherent particle.

The failure strain corresponds to the strain necessary to extend the voids up to a length equal to the particle spacing. When this point is reached, fracture will occur along the grain boundary. In addition, the bulk strain to fracture ε_f (without a pre-crack) depends on the grain size D and the PFZ-width d according to [9]

$$\varepsilon_f = \varepsilon_{ft} + \varepsilon_{fi} \frac{d}{D} \tag{5.2}$$

where ε_{ft} is the portion of strain within the grains. The critical value which determines ε_f can then be either ε_{ft} or ε_{fi}, which in turn depends on the difference in yield stress between the PFZ and the grain interior and therefore on the ageing condition. As the total elongation of the alloy is the sum of the elongations for the grain interior and for the grain boundary regions, the above equation is valid when $d<<D$. If all strain is confined in the soft grain boundary environment, the first term on the right-hand side of the equation can be neglected.

An important parameter governing grain boundary precipitation is the applied cooling-rate after the alloy has been solution heat-treated. It is well known that slack quenches reduce toughness [10-12], especially in recrystallized microstructures where the fraction of random high-angle grain boundaries is much larger. The precipitates tend to be smaller on low-angle grain boundaries because of their smaller free volumes and because of their smaller solute diffusivity that leads to a slower precipitate growth rate. The precipitate-free-zones that circumvent these boundaries are smaller as well. Low-angle grain boundaries have a higher cohesive strength than high-angle grain boundaries, arising from the nature of the grain boundary itself as well as the nature of the interface of the boundary precipitates. In addition, planar slip is expected to traverse more easily the low-angle boundaries because of their small angle of misorientation, which may reduce large stress concentrations at the head of piled-up dislocations. Thus, the high-angle grain boundaries will be most susceptible to crack propagation, as the work needed to advance along them will be less than along low-angle grain boundaries [13].

5.3 PROCESSING ROUTES

AA6061 contains 1.0 at% Mg, 0.7 at% Si, 0.15 at% Cu for precipitation hardening and 0.7 at% Fe, 0.2 at% Cr and 0.15 at% Mn for formation of intermetallic phases. From the as-received (as-extruded) state, two alternative processing routes were applied and these are schematically depicted in Fig 5.2:

- To obtain a recrystallized microstructure, the alloy was cold-rolled with intermediate annealing treatments at 560 °C (reduction in final rolling step ~ 30 %). From the rolled plate, with a thickness of 1.3 mm, tensile specimens without notches were laser-cut according to the dimensions of Fig 5.3. Each specimen was annealed for 35 minutes at 560 °C and was subsequently either water-quenched or air-cooled. Finally, all samples were artificially aged at 160 °C for times ranging up to 112 h. Samples aged for 3 min at 160 °C will be referred to as "as-quenched" from now on. This treatment is applied in order to stabilise the as-cooled alloy [14].

- To preserve the extruded microstructure, plates perpendicular to the extrusion direction with a thickness of 1.3 mm were sawn. Subsequently, tensile specimens were laser-cut. Every specimen was annealed for 35 minutes at 560 °C and was subsequently either water-quenched or air-cooled. Finally, an artificial ageing treatment at 160 °C for 23 h was applied. After this treatment, the typical texture for extruded product was still present. The distribution of the intermetallic phases in this microstructure is found to be much coarser than for the rolled and recrystallized microstructure.

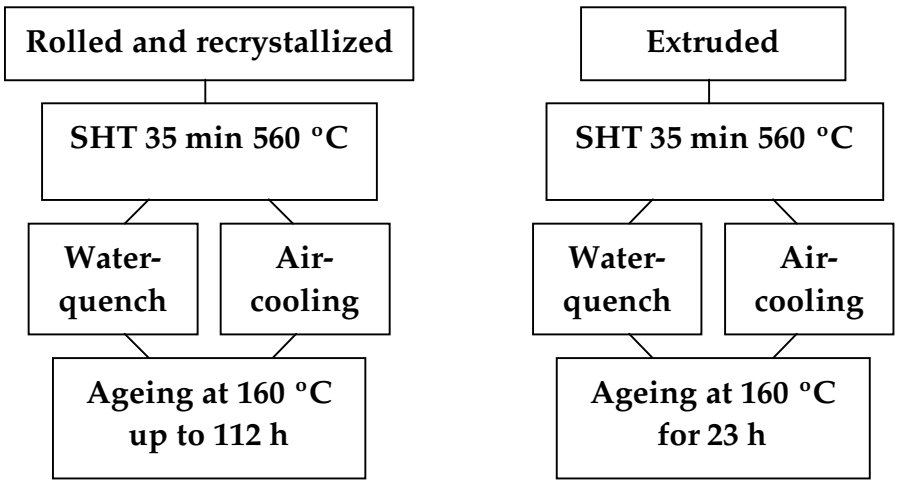

Fig 5.2: *Applied thermomechanical processing routes.*

Of both alternative routes, additional samples for investigation by orientation-imaging microscopy (OIM) or transmission electron microscopy (TEM) were prepared as well.
In this work, all tensile tests are performed at an elongation rate of 10 μm s^{-1}, which using a gage length of 20 mm, corresponds to a strain rate of $5.0 \cdot 10^{-4}$ s^{-1}.

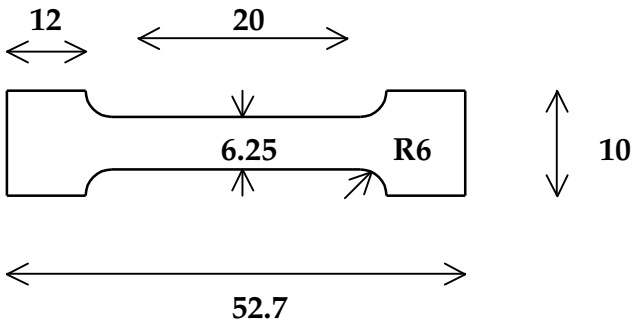

Fig 5.3: *Tensile specimen with dimensions in mm.*

Thickness: 1.3 mm.

5.4 COOLING RATES IN WATER AND IN AIR

As the cooling rate after the solution heat treatment is an important parameter concerning grain boundary precipitation, it is determined for both air-cooled and water-quenched cases. For grain boundary precipitation, the rate of cooling through the regime 450 °C – 250 °C is most important [15]. The driving force for precipitation is the degree of supersaturation, which increases as the temperature decreases. However, the process also depends on the diffusion of solute atoms to nucleation sites and this diffusion rate decreases with decreasing temperature. The precipitation kinetics are thus described by a typical C-curve in the time-temperature-diagram. It is commonly assumed that if the nose of this curve is encountered during slow cooling after solution heat treatment, heterogeneous nucleation occurs leading to large incoherent precipitates with resulting poor mechanical and corrosion properties of the grain boundary.

The cooling curve is determined according to the method described in Chapter 2. For the water-quenched case, the cooling-rate is only calculated, as it is difficult to measure accurately the sharp temperature drop with time. The heat transfer coefficient for water will be taken equal to 40 kW m^{-2} $°K^{-1}$. Fig 5.4a depicts the modelled temperature versus time for a 1.3 mm-thick tensile specimen that is quenched in water at room temperature. The average cooling rate through the critical range of 450-250 °C can be determined equal to $1.09 \cdot 10^{4}$ °C s^{-1}.

For the air-cooled case, the cooling-rate can also be measured experimentally by putting a thermocouple on the sample surface immediately after it has left the furnace. The measured temperature decrease from 560 °C with time is given in Fig 5.4b. Also in this figure is the calculated cooling rate of a 1.3 mm-thick sample, using 10 W m^{-2} $°K^{-1}$ for the heat transfer coefficient of still air. The average cooling rate through the critical range of 450-250 °C is calculated to be 2.7 °C s^{-1}. As can be observed in the figure, the predicted and experimental curves for air-cooling are in reasonable agreement.

5.5 MECHANICAL TESTING

5.5.1 Influence of cooling rate, artificial ageing time and microstructure

The stress-strain curves of both water-quenched and air-cooled recrystallized alloys are depicted in Figs 5.5a and 5.5b, respectively, for different times of artificial ageing at 160 °C. Each curve is the average of two independent measurements. From Fig 5.5a, it can be seen that for the water-quenched alloy the strength first increases up to the point of peak strength (at 23 h) and subsequently decreases again with ageing time (i.e. over-ageing). The fracture strain monotonically decreases with ageing time. These observations are to be expected for precipitation-hardened alloys. The strength of the air-cooled alloy (Fig 5.5b), although somewhat smaller in magnitude, shows the same trend with ageing time as that of water-quenched product. The interesting part however, is the fracture strain, which first exhibits a local minimum at about 5 h of ageing before increasing again to a local maximum in the range 23 h – 112 h.

Extruded material, water-quenched or air-cooled, was aged for 23 h at 160 °C and tested in tension at the same strain rate. The stress-strain curves, which are again the average of two independent measurements, are depicted in Fig 5.6. The difference in strength between the water-quenched and air-cooled alloys is comparable to that of the recrystallized microstructure, whereas the fracture strain can be seen to be much smaller than that of recrystallized product for both cases. In addition, a large fracture strain difference (~ 4.5 %) between the water-quenched and air-cooled alloy is prevalent, whereas the fracture strains of the water-quenched and air-cooled recrystallized microstructures are comparable after 23 h of ageing.

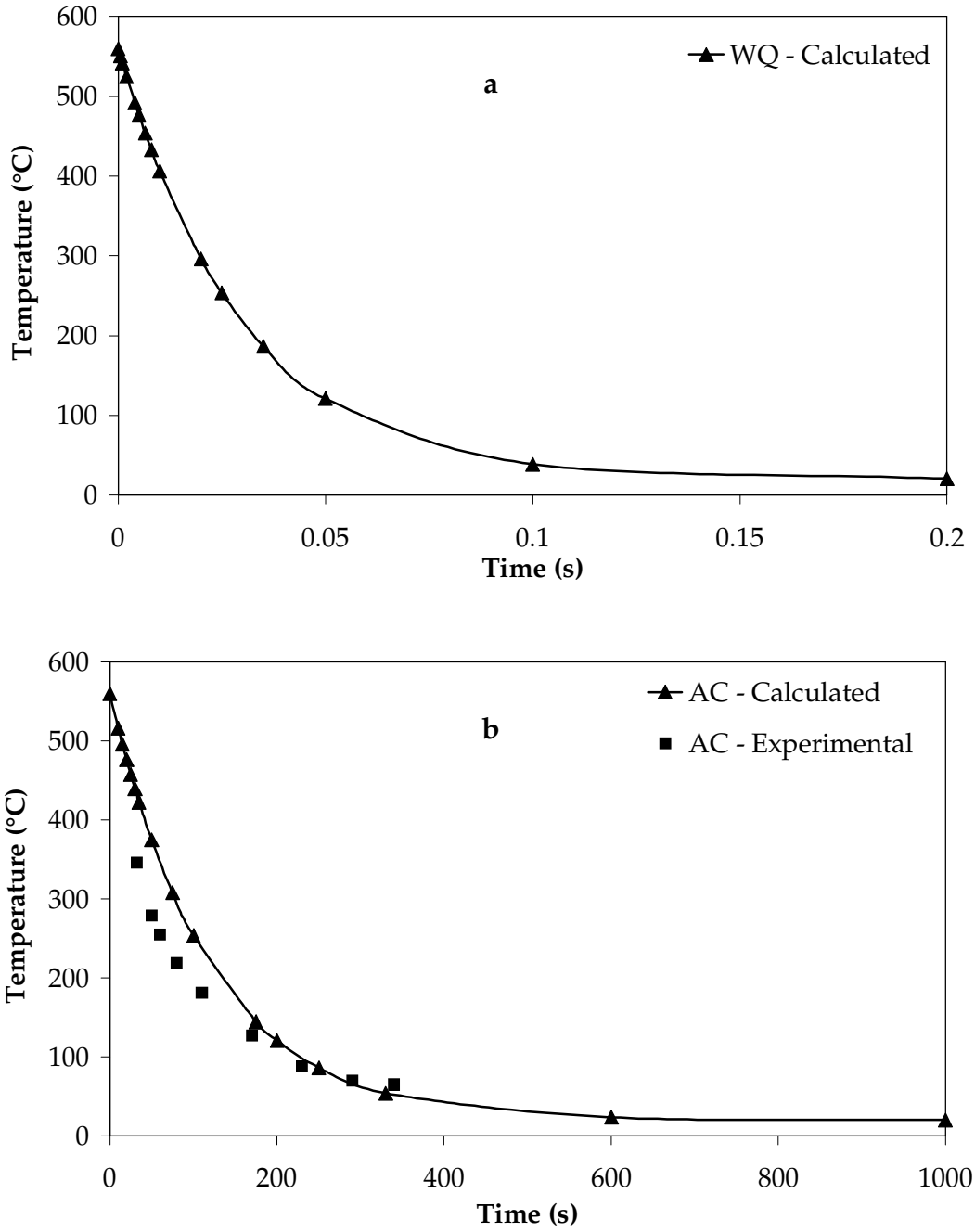

Fig 5.4: *Cooling rates for 1.3 mm-thick AA6061 alloy:*
(a) Water-quenched
(b) Air-cooled

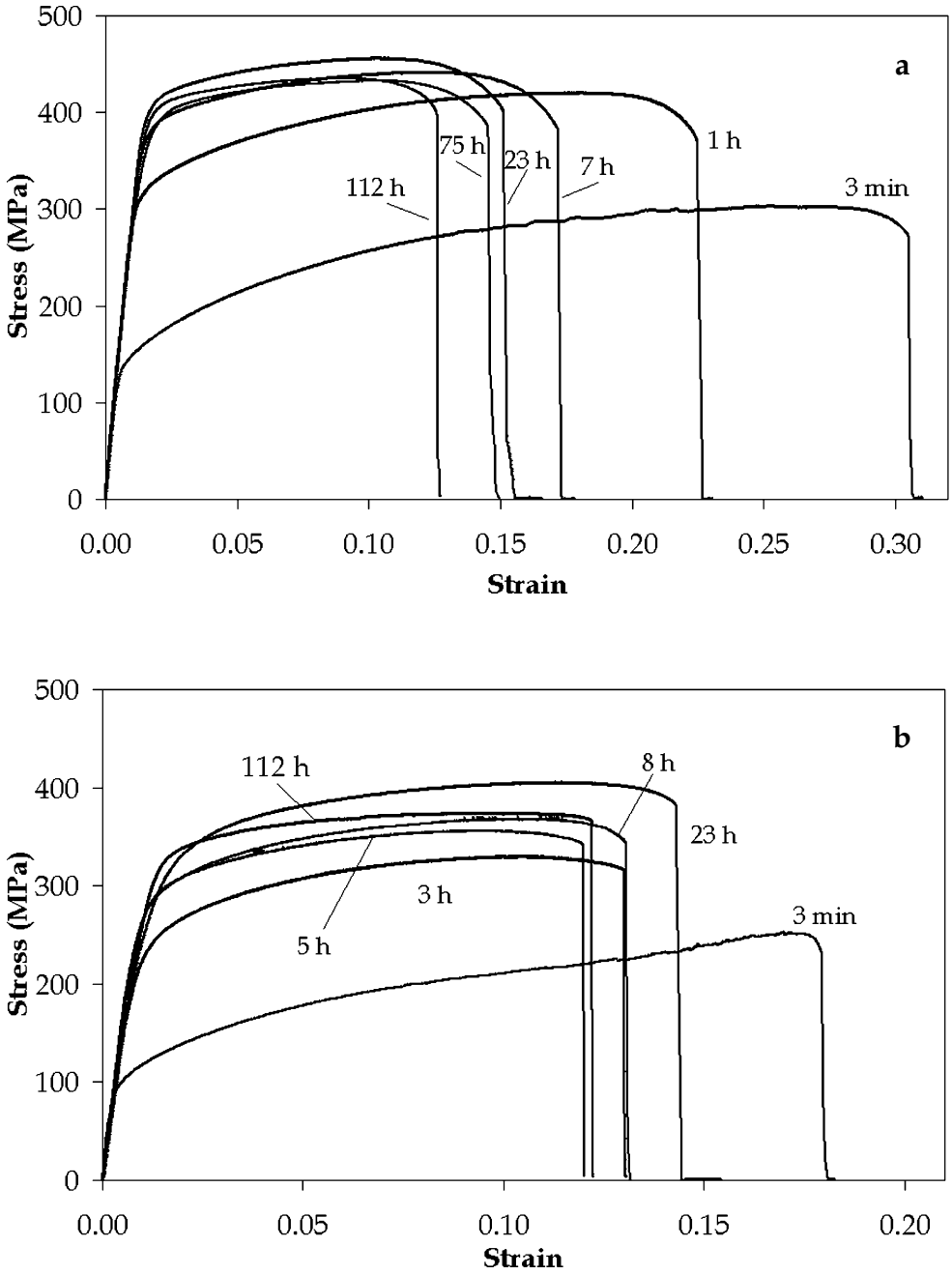

Fig 5.5: *Stress-strain diagrams of AA6061 with recrystallized microstructure at different states of artificial ageing:*
(a) Water-quenched
(b) Air-cooled

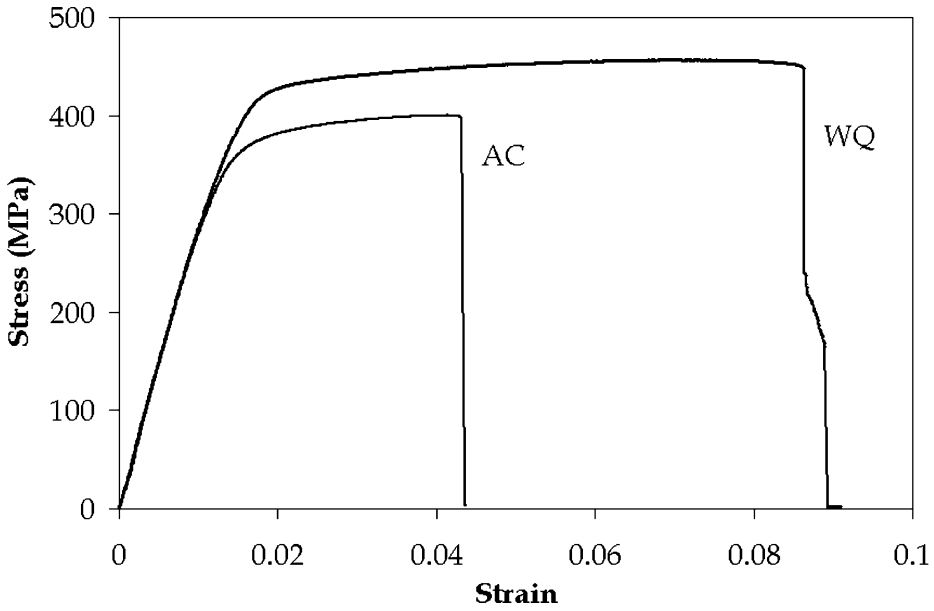

Fig 5.6: *Stress-strain diagrams of AA6061 with extruded microstructure subjected to different cooling rates and aged for 23 h at 160 °C. (WQ – water-quenched, AC – air-cooled)*

5.5.2 Fractographic analysis

Recrystallized microstructure

After the samples were tested in tension, their fracture surface was examined in a scanning electron microscope. To obtain better insight into the fracture mechanism of both water-quenched and air-cooled alloy after different times of artificial ageing at 160 °C, the fracture surfaces of samples in underaged, peak-aged and overaged conditions are compared in Fig 5.7.

For the water-quenched alloy, the uniform strain to fracture monotonically decreases during ageing, but the ductility (as measured from the aspect of the fracture surfaces) first increases from the underaged to the peak-aged state and then decreases again in the overaged microstructure (Figs 5.7a-c). The fracture mode is mainly according to transgranular-microvoid coalescence and the fraction of intergranular-microvoid-coalescence is largest in the peak-aged condition. As can be seen in Fig 5.7a, for the underaged alloy, relatively flat shear zones connect the dimples. As ageing proceeds the fracture surface

between the large dimples becomes covered by smaller dimples. Also the portion of intergranular failure increases (Fig 5.7b) because the difference in yield stress between grain boundary region and grain interior increases accordingly. As the grain size and the distribution of intermetallic phases both remain unaltered during artificial ageing, the change in mechanical response can be attributed solely to changes in matrix- and grain boundary precipitation. In the underaged state, the precipitates are still coherent with the matrix and can therefore be cut by moving dislocations, leading to an effective softening of slip planes and consequent formation of intense slip bands [16], which may favour shear-fracture. On the contrary, in the peak-aged condition a significant proportion of the needles is by-passed by an Orowan mechanism [7] and the resistance to shearing is increased, which enhances ductility. As matrix precipitation coarsens during over-aging, the tendency for shear-fracture increases again, which is evident from Fig 5.7c. Here the fracture surface consists mainly of flat shear zones and regions of intergranular failure.

From Fig 5.7d it can be observed that the fracture mechanism of the underaged air-cooled sample is predominantly of a ductile transgranular type with regions of shear, whereas the 23 h-aged sample seems to have failed mainly according to a ductile intergranular fracture mode (Fig 5.7e). Apparently, a transition from ductile transgranular- to ductile intergranular fracture mode sets in with artificial ageing time, which can be explained by the increase in yield stress difference between grain boundary zone and grain interior with ageing time until peak-strength is achieved. In this way plastic deformation may become located to a larger degree at the relatively soft grain boundary region. For the overaged state (Fig 5.7f), the fraction of intergranular failure has slightly decreased, just as for the water-quenched case. The amount of shear fracture is however much smaller than that of the water-quenched alloy aged for the same time (Fig 5.7c), which may indicate that the strain remains more confined to the grain boundary region.

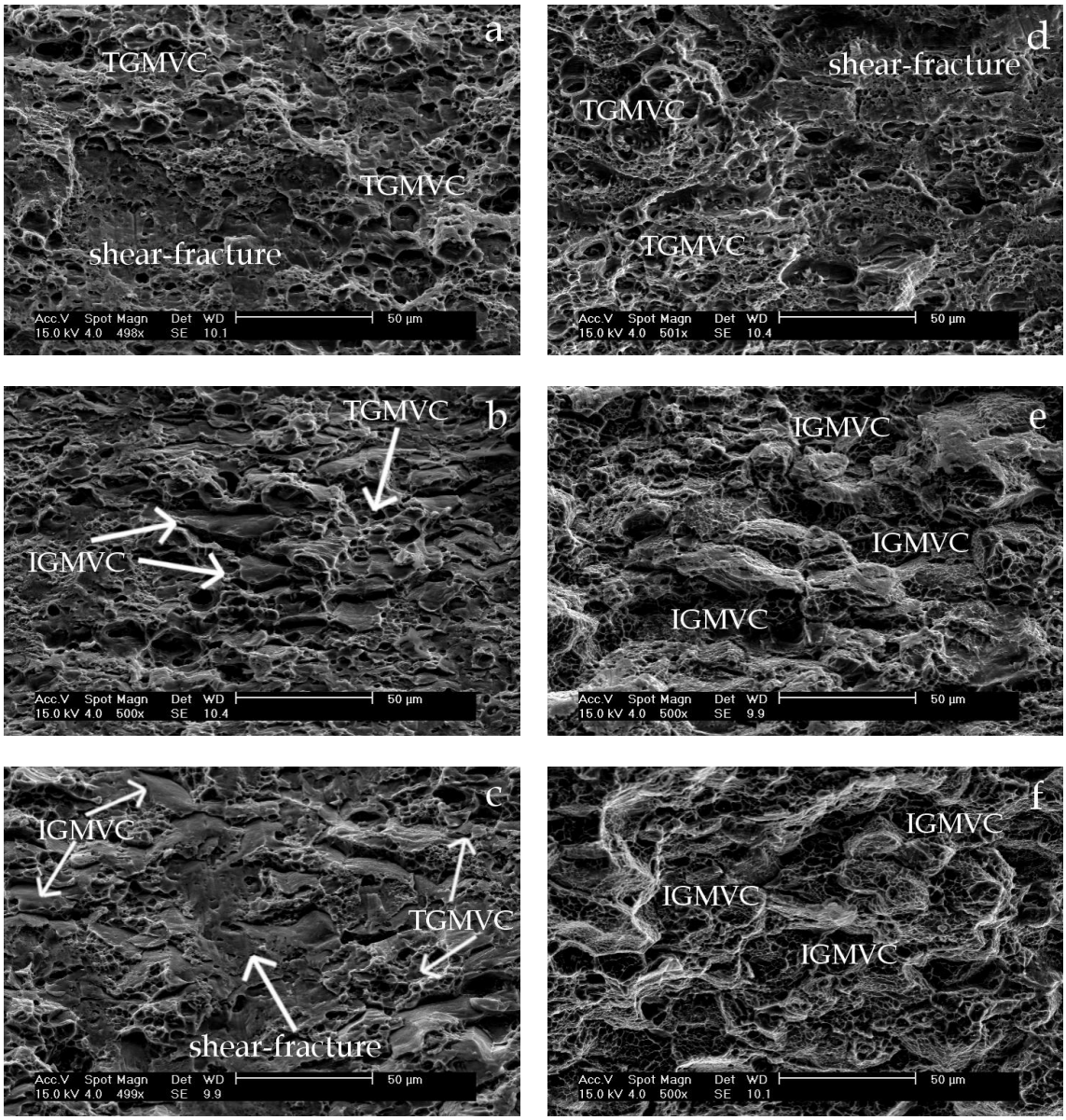

Fig 5.7: *Fracture surfaces (500x) of recrystallized AA6061 water-quenched (WQ) or air-cooled (AC) and subsequently aged at 160 °C for different times:*
(a) WQ – 3 min (b) WQ – 23 h (c) WQ – 112 h
(d) AC – 3 min (e) AC – 23 h (f) AC – 112 h
TGMVC – Transgranular microvoid coalescence
IGMVC – Intergranular microvoid coalescence

As mentioned earlier, the influence of the properties of the grain boundary region on fracture strain is largest when the difference between yield stress of grain boundary region and grain interior is largest (i.e. in the peak-aged condition). The concentration of plastic deformation in the grain boundary region will then be largest. In Figs 5.8a and 5.8b, respectively, intergranular fracture surfaces of water-quenched and air-cooled alloys in peak-aged condition (i.e. 23 h at 160 °C) are compared at high magnification. The amount of plastic deformation in the grain boundary region, as measured by cusp-depth, can clearly be seen to be much smaller for the water-quenched case.

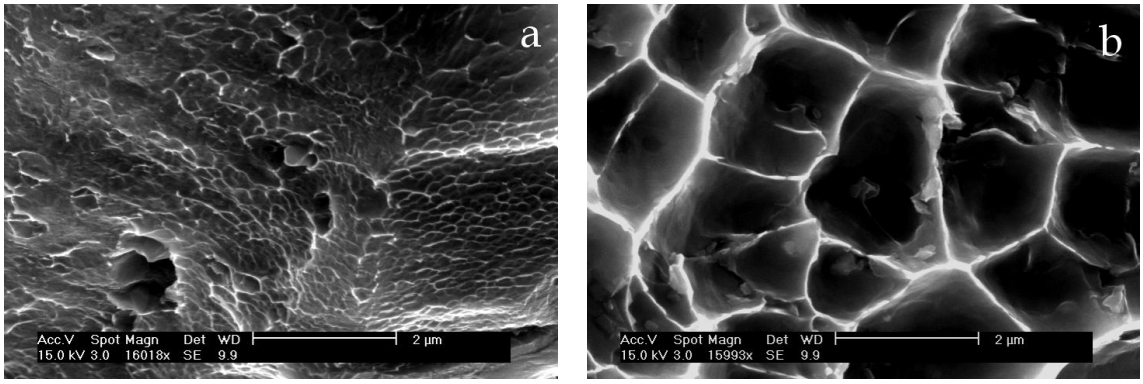

Fig 5.8: *Intergranular fracture surfaces (16000x) of recrystallized AA6061 water-quenched or air-cooled and aged to peak strength:*
(a) Water-quenched (b) Air-cooled

Extruded microstructure

Samples with an extruded microstructure at peak-strength were tested in tension under similar conditions as for the recrystallized samples. The fracture surfaces for water-quenched and air-cooled product are presented in Figs 5.9a-c and 5.9d-f, respectively. The total fraction of intergranular failure for both cooling rates is notably smaller than for the recrystallized microstructure aged to the same condition (Figs 5.9a,d vs. 5.7b,e). Comparing Figs 5.9c,f to 5.8a,b, it can be seen that cusp-size and -depth at the intergranular fracture surfaces are again largest for the air-cooled alloy and comparable to those of the recrystallized microstructure.

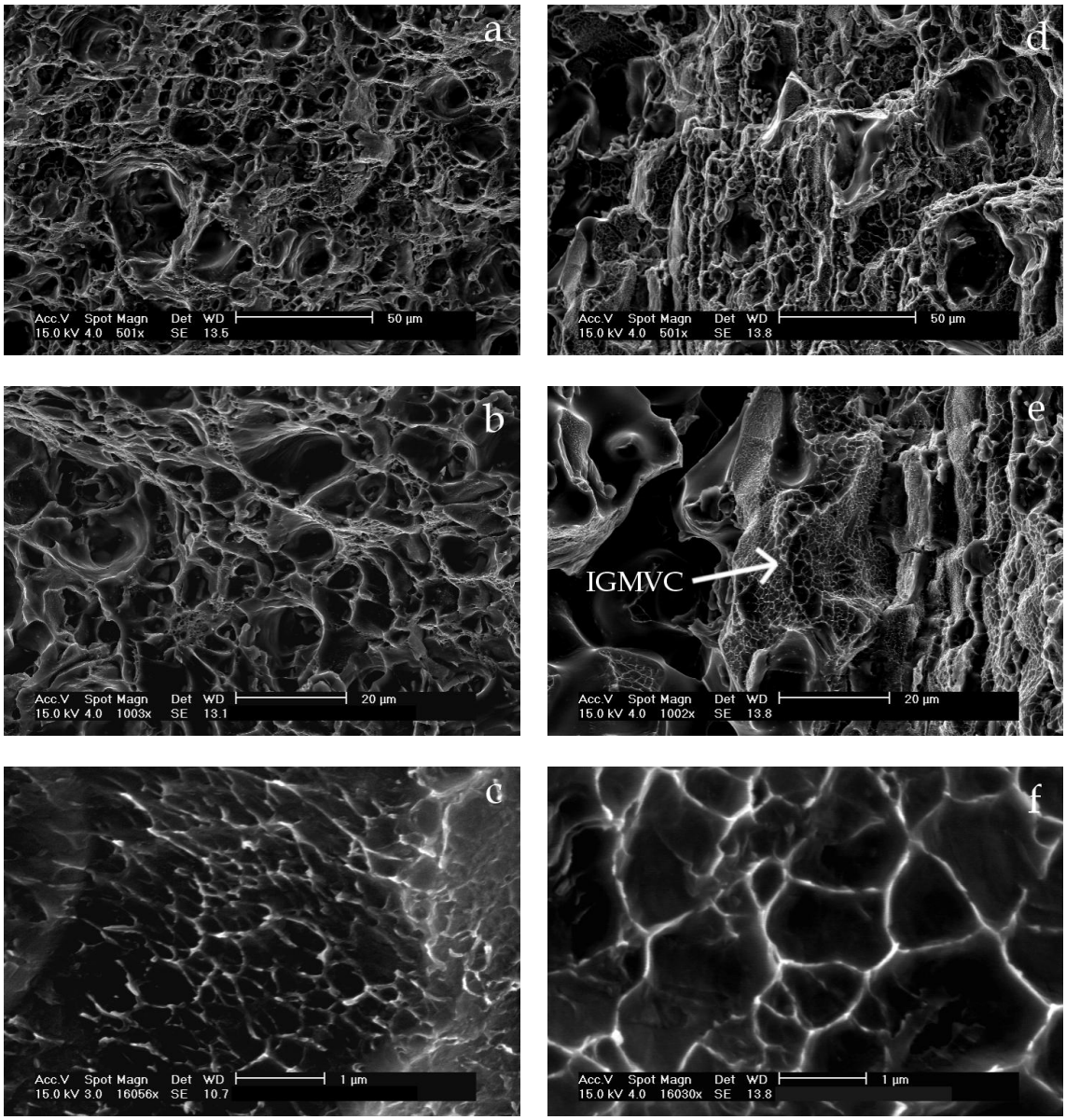

Fig 5.9: *Fracture surfaces of extruded AA6061 water-quenched (WQ) or air-cooled (AC) and subsequently aged to peak strength (23 h at 160 ºC): (a) WQ – 500x (b) WQ – 1000x (c) WQ – 16000x (d) AC – 500x (e) AC – 1000x (f) AC – 16000x IGMVC – Intergranular microvoid coalescence*

5.6 GRAIN BOUNDARY PRECIPITATION

In Figs 5.10a,b, transmission electron micrographs are presented of random high-angle grain boundaries in an air-cooled sample aged to peak-strength. These figures give a reasonable indication of the grain boundary precipitate size and inter-distance for the air-cooled alloy. The size varies between 0.5 μm and 2 μm and the centre-to-centre distance between the phases is about 0.7 μm, which compares to the sizes of the dimples observed on top of the intergranular facets (~ 1 – 2 μm, from Fig 5.8b). Comparing Fig 5.10a to 5.10c, the width of the precipitate-free-zones around random high-angle grain boundaries can be determined to be about 35 nm and 280 nm for water-quenched and air-cooled alloys, respectively. Fig 5.10d depicts a dark-field micrograph of a low-angle grain boundary (5 º on a <111>) in extruded product aged to peak strength. Grain boundary precipitation is not resolved and the width of the precipitate-free-zone is negligible, indicating a very small amount of solute segregation to this grain boundary during the quench.

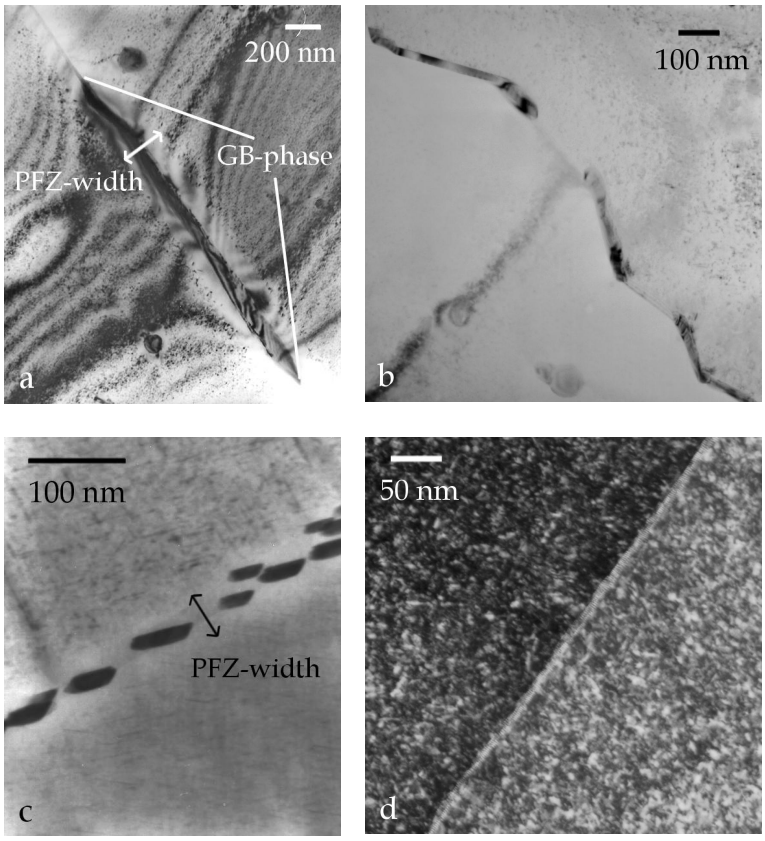

Fig 5.10:
Grain boundary precipitation and PFZ-widths in AA6061:

(a), (b) Recrystallized, air-cooled, aged 23 h at 160 ºC. General GB

(c) Recrystallized, water-quenched, aged 50 h at 160 ºC. General GB

(d) Extruded, water-quenched, aged 23 h at 160 ºC. Low-angle GB (Dark-field image)

5.7 DISCUSSION

5.7.1 Recrystallized microstructure

Underaged condition

As the fracture mode of both water-quenched and air-cooled material without artificial ageing is mainly transgranular, the bulk fracture strain cannot directly be related to precipitation at grain boundaries or grain boundary fracture energy. In this condition, the fracture mechanism can be described by initiation of voids at the interfaces between the intermetallic phases and the matrix. As can be observed by comparing Fig 5.5a to 5.5b, the fracture strain for the as-air-cooled alloy is much smaller than for the as-water-quenched sample (i.e. 18 % vs. 31 %). Because both the grain size and the size and distribution of the matrix intermetallic phases in both alloys are comparable (i.e. apart from the cooling rate they were both subjected to identical processing routes), the only differences present in the air-cooled alloy are heterogeneous precipitate nucleation at the intermetallics and extensive grain boundary precipitation. The latter is most likely to be responsible for the smaller fracture strain. Although fracture is not of intergranular type in this state, voids may form at the large grain boundary phases nucleated during air-cooling, and these may assist in the link-up of voids that nucleated at intermetallic phases within the interior of the grains (schematically depicted in Fig 5.11). Because of the large grain boundary phases, slip transmission across the boundary will also be more obstructed for the air-cooled alloy and consequently, the fracture strain may be reduced significantly with respect to that of the water-quenched alloy.

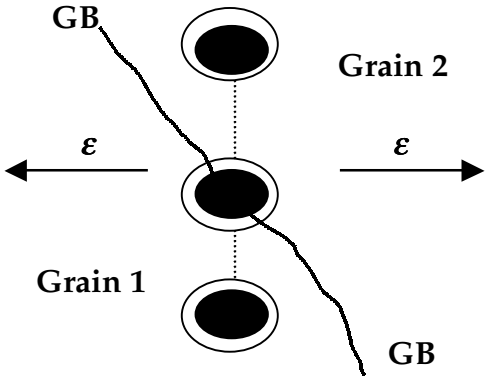

Fig 5.11: *Void nucleated at grain boundary phase may assist in link-up of voids nucleated at intermetallic phases in the grain-interiors.*

Fracture energy versus cooling-rate and amount of artificial ageing

Fig 5.12a depicts the fracture energies for different ageing times, determined by integrating the area under the stress-strain curves in the plastic regime. From this figure, it can be seen that the fracture energy for the air-cooled alloy first increases slightly with ageing time, just as for the water quenched case. This initial rise is mainly the result of an increase in yield stress. Starting from the point of maximum fracture energy, a significant difference between the water-quenched and the air-cooled alloy is apparent; the fracture energy of the water-quenched alloy further decreases with ageing time, whereas for the air-cooled alloy it first decreases, reaches a local minimum after about 5 h of ageing and then increases again to a next local maximum. When only the fracture strain is plotted against ageing time (Fig 5.12b), it can be observed that, except for underaged state, the shape of the fracture energy curve of both alloys is mainly affected by the fracture strain. For the air-cooled case, this strain is predominantly controlled by grain boundary properties in a broad range around the peak-aged condition. This can be validated when the fracture surfaces of the air-cooled alloy for different times of ageing are considered (Figs 5.7d-f). Here it can be observed that, except for the extreme underaged case, the fracture mode is predominantly of ductile intergranular nature, whereas for the water-quenched alloy a much larger portion of transgranular fracture is observed (Figs 5.7a-c). For the air-cooled alloy, a larger degree of correlation thus exists between the fracture strain and the properties of the grain boundary region, possibly explaining the observed difference in trend in fracture energy for both cooling-rates.

The observed trend for the fracture strain of the air-cooled alloy can be explained by: 1. the degree of strain-concentration in the grain boundary region and 2. the altering grain boundary volume fraction of precipitates.
During the first stages of ageing, the grain boundary precipitates grow (Fig 5.13a,b), aided by both the remaining grain boundary solute-concentration and the solute-supply from the grain interior. Because of precipitate growth, the precipitate volume fraction in the PFZ increases and from equation (5.1) it can be seen that this will decrease the local critical fracture strain. Apparently, this effect is so pronounced that it affects the bulk fracture strain as well. This can be understood, because the strain also becomes more confined to the grain boundary region with ageing time up to peak-aged condition (Figs 5.7d-e).

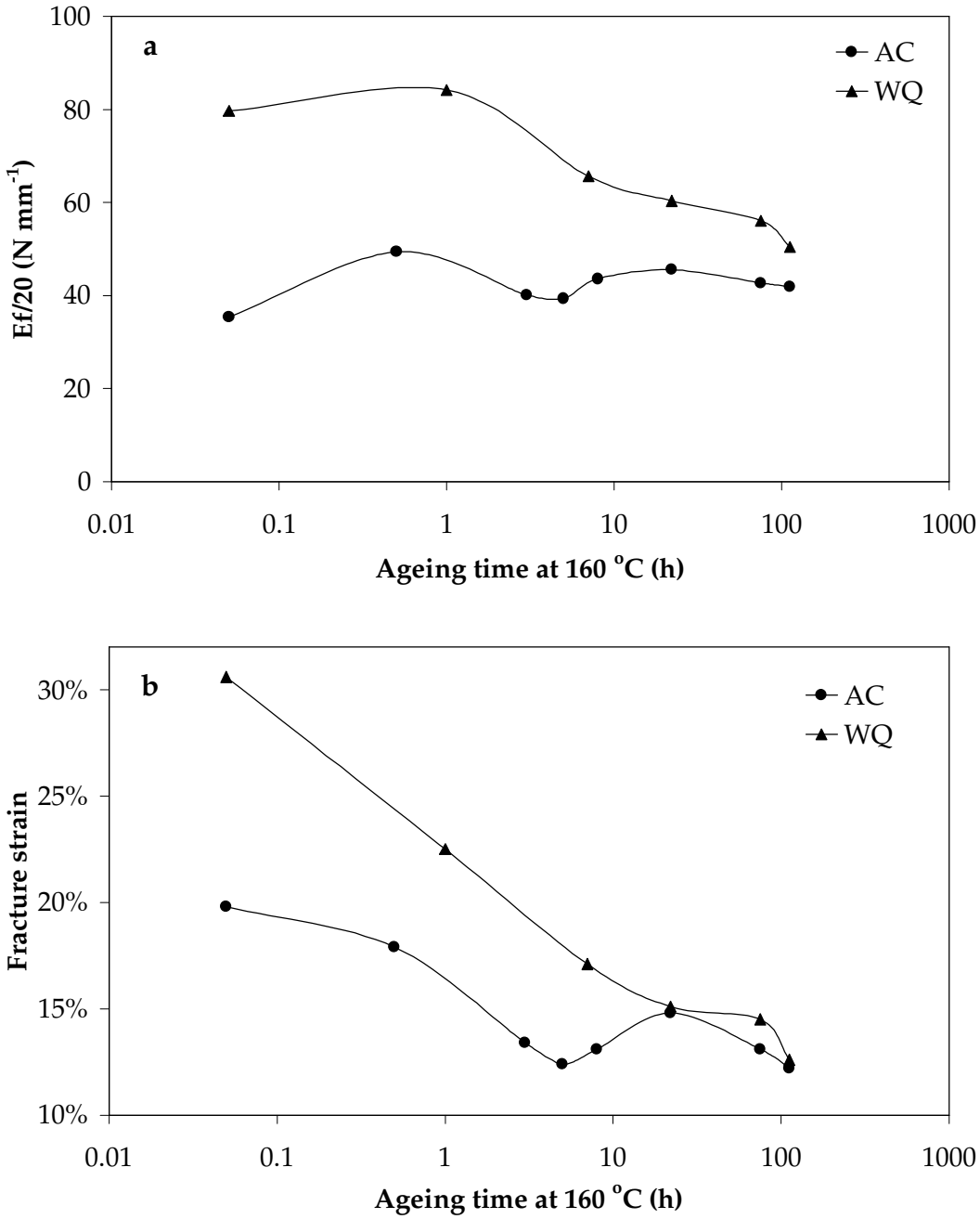

Fig 5.12: *Mechanical response of water-quenched (WQ) and air-cooled (AC) AA6061 alloy:*
(a) Fracture energy against artificial ageing time at 160 °C
(b) Fracture strain against artificial ageing time at 160 °C

After ageing for longer times, the solute supply to the grain boundary becomes exhausted and the grain boundary phases start to coarsen (Fig 5.13b,c). This may decrease their local volume fraction and according to equation (5.1) the critical fracture strain at the grain boundary will then increase. Because of the larger mean distance between the grain boundary precipitates, the linkage of the intergranular voids, nucleated at these precipitates, will occur at a later stage. In addition, slip transmission across the grain boundary may become easier and therefore the transgranular fracture strain may increase as well. According to equation (5.2), an increase in the bulk fracture strain is then obtained. The observed minimum in fracture strain for the air-cooled sample can therefore be explained by growth and subsequent onset of coarsening of the grain boundary phases with ageing time.

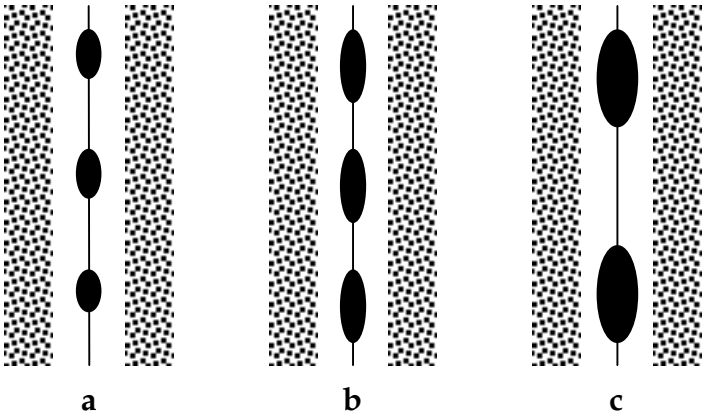

Fig 5.13:
Grain boundary precipitate distribution during artificial ageing of air-cooled sample. From (a) to (b) – growth From (b) to (c) - coarsening

The description above is further supported by experimentally measured cusp-size distributions resulting from void coalescence at the grain boundary, presented in Fig 5.14. Only cusps from voids that formed at grain boundaries perpendicular to the applied load were considered, because for other grain boundary orientations the influence of shear on cusp-shape may be considerable. In the figure the effect of coarsening, which sets in after about 5 h of ageing judging from the fracture-strain diagram (Fig 5.12b), is reflected in a shift of the cusp-size distribution to larger sizes when the ageing time is increased to 23 h. The average critical void size at fracture increases from 1.74 μm to 1.97 μm, which may explain the increase in fracture strain [17].

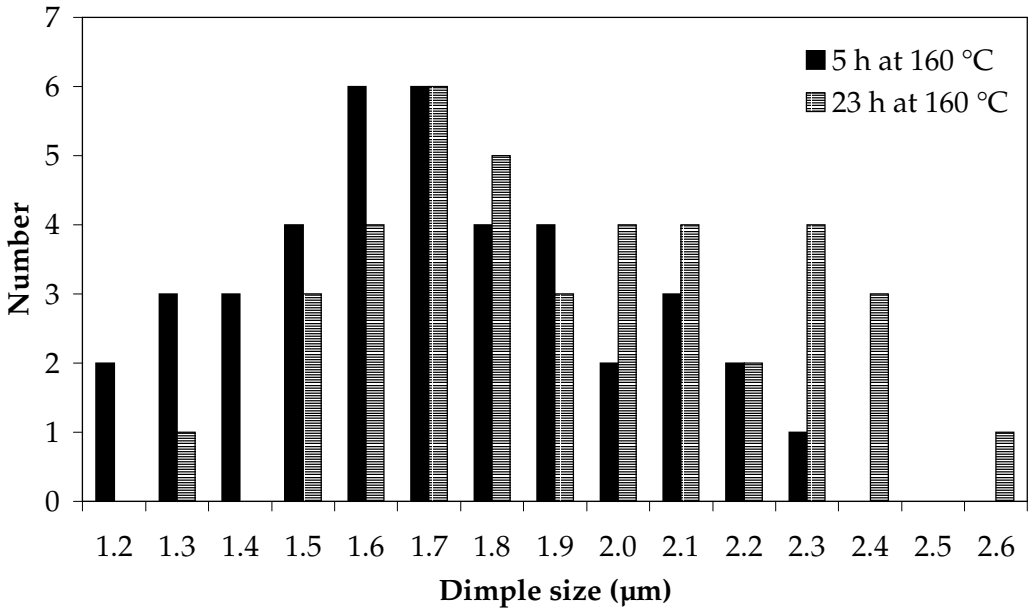

Fig 5.14: *Intergranular cusp-size distributions for air-cooled product artificially aged for 5 h and 23 h at 160 °C.*

Subsequently, the fracture strain exhibits a next local maximum and decreases again after 23 h of ageing. This maximum may find its origin in coarsening of *matrix* precipitates during overageing. Beyond the peak-aged condition, matrix slip may become more localized again, increasing the tendency for shear- and intergranular fracture. Because the difference in hardness between the grain boundary region and the grain interior decreases again, strain confinement to the grain boundary region decreases as well and a net decrease of the bulk fracture strain may be the result.

With artificial ageing of the water-quenched alloy, the grain boundary precipitates nucleate and grow, providing an increasing barrier to slip transmission across the boundary. In addition, plastic strain becomes more confined to the grain boundary region with ageing time, whereas void formation becomes easier at the growing grain boundary precipitates [18]. Above processes may well explain the increasing fraction of intergranular fracture with ageing to peak-aged condition (Figs 5.7a,b), contributing to a continuous decrease of the bulk fracture strain (Fig 5.12b). After peak-aged condition is reached, coarsening of matrix precipitates results in more localized matrix slip and the tendency for shear fracture increases again (Fig 5.7c). This contributes to a further decrease in bulk fracture strain, just as was observed for

the air-cooled alloy. The fracture strain of the alloy aged for 75 h is slightly larger than would be expected from the general trend of the curve. Apparently, coarsening of the grain boundary precipitates, which occurs at a later stage in the water-quenched alloy, may still be reflected in the bulk fracture strain. However, since the strain-confinement to the grain boundary region may not be as extensive as for the air-cooled alloy (because the PFZ-width is smaller), the effect is not so pronounced and does not lead to a local maximum.

Intercrystalline and transcrystalline strain at peak-aged condition

As the percentage of intergranular failure is largest in the peak-aged condition for both water-quenched and air-cooled recrystallized product, the grain boundary properties can best be correlated to the bulk mechanical properties at this point. From Fig 5.12b, the bulk fracture strains of both cooling-rates can be seen to be about equal (~ 15 %) after 23 h of artificial ageing. Of this bulk fracture strain, the amount of strain confined to the grain boundary region for both cooling rates will be determined below.

As determined from the TEM-micrographs (Figs 5.10a,c), the precipitate-free zone widths are 35 nm and 280 nm for the water-quenched and air-cooled alloys, respectively. Using the grain boundary precipitation model [19,20] described in Chapter 4, the volume fraction of grain boundary precipitates in the precipitate free zone in peak-aged condition was calculated to be ~ 6.4 % for the water-quenched alloy. As this model is based on non-equilibrium segregation conditions and as it considers segregation and precipitation as two separate processes, it may not be valid for the air-cooled case, because of the slow cooling-rate and precipitation during cooling. Direct determination of grain boundary precipitate volume fraction in the precipitate-free-zone from TEM-micrographs is not very accurate and thus it is derived from the average intergranular cusp-size of the fracture surface. According to Broek [21], a linear relationship between cusp-size and particle spacing exists. The average cusp-size of the air-cooled sample aged for 23 h, was found to be ~ 2 μm in both orthogonal directions lying on the grain boundary plane, which would imply a particle spacing of ~ 1 μm according to the above reference. This value is comparable to the observed interdistance in Fig 5.10b. Together with the observed particle size and the PFZ-width, this corresponds to a grain boundary precipitate volume fraction of ~ 4.5 % for the air-cooled alloy. At first sight it may seem contradictory that this value is smaller than that for the water-quenched case, but it can be explained by the

much wider PFZ for the air-cooled alloy. For the present volume fractions, the critical strain for void nucleation ε_n in equation (5.1) is found to have a minor influence on the intergranular fracture strain ε_{fi} and it is assumed to be equal to the strain at yielding (i.e. ~1.4 % for both cases). As the precipitate volume fraction for the air-cooled alloy is smaller and because the PFZ-width is larger by a factor 8, the total fraction of strain localized to the grain boundary region is largest for the air-cooled alloy. From equation (5.1), the PFZ-confined strains can be determined to be 61.7 % and 89.5 % for the water-quenched and air-cooled alloy, respectively, which may explain the larger fraction of intergranular fracture and the larger amount of localized plastic deformation (Figs 5.8a,b) for the air-cooled alloy. After substitution of the average grain size (~14 μm) and the PFZ-widths in equation (5.2), the *transgranular* strains for water-quenched and air-cooled product are 14.8 % and 13.2 %, respectively.

5.7.2 Comparison of recrystallized and extruded microstructure at peak-strength

From the stress-strain curves, the strengths of the extruded water-quenched and air-cooled samples are 450 MPa and 400 MPa, respectively and thus comparable to the peak-aged strengths of recrystallized material. On the contrary, the fracture strain of peak-aged extruded material is much smaller than that of recrystallized material; 8.6 % and 4.3 % for extruded water-quenched and air-cooled alloys respectively vs. ~ 15 % for the recrystallized alloy. As the grain size distribution is comparable for both microstructures (Fig 5.15), this cannot explain the observed difference in mechanical properties.

The smaller strain to fracture with respect to the recrystallized alloy may be explained by a much coarser distribution of intermetallic phases in the extruded microstructure. For the recrystallized microstructure, this distribution is more refined during cold-rolling. A finer distribution to a greater extent prevents localization of slip [22], so that the fracture mode will be more ductile in nature. More extensive slip localization in the extruded alloy on the other hand, increases shear band formation as well as stresses ahead of the pile-ups acting on the grain boundary region, both reducing the fracture strain [16,22]. Regarding on the other hand the fracture surfaces of the extruded alloy (Fig 5.9), it is clear that the fraction of intergranular failure for both water-quenched and air-cooled extruded alloy is significantly smaller than for the recrystallized alloy (Fig 5.7). This can be explained by the larger fraction of low-angle grain boundaries in extruded material with respect to recrystallized material, presented in Fig 5.16.

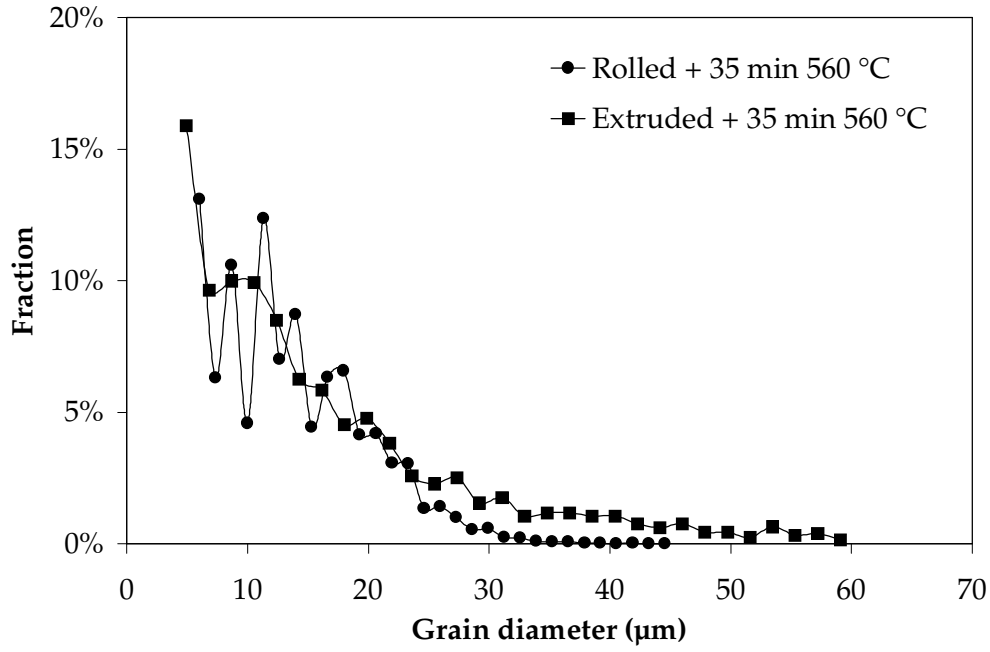

Fig 5.15: *Grain size distributions for AA6061 with recrystallized and extruded microstructure.*

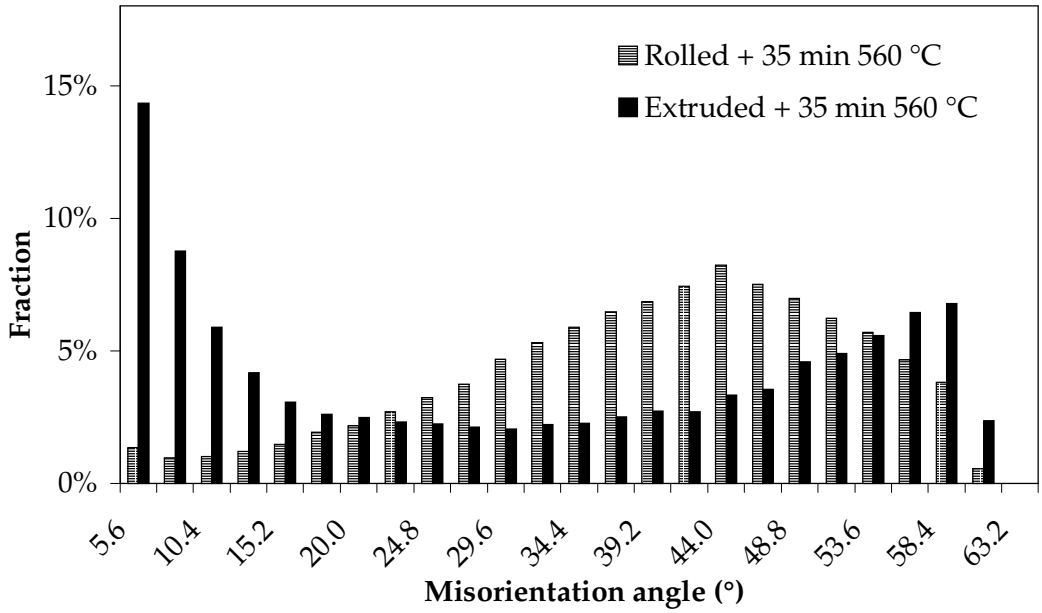

Fig 5.16: *Grain boundary misorientation angle distributions for AA6061 with recrystallized and extruded microstructure.*

Segregation to, and precipitation at this type of boundaries are less pronounced, their precipitate free zones are smaller (Fig 5.10d), their cohesive strength is larger and slip transmission is easier. Plastic deformation thus will be less concentrated at these grain boundaries, rendering a larger fraction of transgranular fracture for the extruded microstructure.

Considering fracture behaviour for the extruded microstructure subjected to different cooling rates, the fraction of intergranular fracture for the air-cooled alloy can be seen to be significantly larger than that for the water-quenched alloy (Figs 5.9b,e). This may affect bulk fracture and may thus explain the large difference in fracture strain between the two alternative cooling-rates. The difference between fraction intergranular failure of air-cooled and water-quenched material with a recrystallized microstructure at peak-strength is smaller (Figs 5.7b,e) and consequently the difference in fracture strain is also smaller.

5.8 CONCLUSIONS

Large grain boundary particles in the as-quenched state may result in much smaller fracture strains.

Much wider precipitate free zones and smaller grain boundary precipitate volume fractions for the air-cooled alloy may explain the larger fraction of strain confined to the grain boundary region as compared to the water-quenched alloy.

By confinement of strain to the grain boundary region, properties such as growth and coarsening of the grain boundary precipitates are reflected in the bulk fracture strain.

A much coarser distribution of intermetallic phases in the extruded microstructure is responsible for larger degrees of slip localization. This enhances the tendency for shear- and intergranular fracture, reducing the ductility and thus the fracture strain with respect to that of the recrystallized microstructure. Although slip localization is more pronounced, the larger amount of low-angle grain boundaries in extruded product decreases the fraction of ductile intergranular fracture significantly with respect to the recrystallized structure.

REFERENCES

1. Thompson, D.S., *Met. Trans.*, **6A**, 671 (1975)
2. Morere, B., Ehrström, J.C., Sinclair, I., *Met. Trans.*, **31A**, 2503 (2000)
3. Bhattamishra, A.K., Lal, K., *Materials & Design*, **18**, 25 (1997)
4. ASM Metals Handbook, 9th edition Vol 12, Fractography, ASM international, 1987
5. Wray, P.J., *Met. Trans.*, **A15**, 2059 (1984)
6. Brown, L.M., Embury. J.D., *Proc. 3rd ICSMA*, **1**, 164, Cambridge (1973)
7. Urreta, S.E., Louchet, F.,Ghilarducci, A., *Mat. Sci. Eng.*, **A302**, 300 (2001)
8. Gräf, M., Hornbogen, E., *Acta Metall.*, **25**, 877 (1977)
9. Gräf, M., Hornbogen, E., *Acta Metall.*, **25**, 883 (1977)
10. Schwellinger, P., *Aluminium*, **55**, 136 (1979)
11. Dorward, R.C., Bouvier, C., *Mat. Sci. Eng.*, **A254**, 33 (1998)
12. Dorward, R.C., Beerntsen, D.J., *Met. Trans.*, **26A**, 2481 (1995)
13. Bryant, A.J., Thomas, A.T., *J. Inst. Met.*, **100**, 40 (1972)
14. L. Zhen, S.B. Kang, H.W. Kim, *Mat. Sci. Tech.*, **13**, 905 (1997)
15. Sheppard, T., *Extrusion of aluminium alloys*, Kluwer Academic Publishers, Dordrecht (1999)
16. Dowling, J.M., Martin J.W., *Acta Metall.*, **24**, 1147 (1976)
17. Kawabata, T., Izumi, O., *Journal of Materials Science*, **11**, 892 (1976)
18. Tanaka, K., Mori, T., Nakamura, T., *Phil. Mag.*, **21**, 267 (1970)
19. Jiang, H., Faulkner, R.G., *Acta Mater.*, **44**, 1857 (1996)
20. De Haas, M., De Hosson, J.Th.M., *Scripta Mater.*, **44**, 281 (2001)
21. Broek, D., *Enging. Fracture Mech.*, **5**, 55 (1973)
22. Blind, J.A., Martin, J.W., *Mat. Sci. Eng.*, **57**, 49 (1983)